Evaluation of low-cost oxygen carriers for biomass chemical looping gasification

Goel, Avishek; Ismailov, Arnold ; Moghaddam, Elyas M.; He, Chao; Konttinen, Jukka

DOI
10.1016/j.cej.2023.143948

Publication date
2023

Document Version
Final published version

Published in
Chemical Engineering Journal

Chemical Engineering Journal 469 (2023) 143948

Contents lists available at ScienceDirect

Chemical Engineering Journal

journal homepage: www.elsevier.com/locate/cej

Evaluation of low-cost oxygen carriers for biomass chemical looping gasification

Avishek Goel [a], Arnold Ismailov [a], Elyas M. Moghaddam [b], Chao He [a,*], Jukka Konttinen [a]

[a] Materials Science and Environmental Engineering, Faculty of Engineering and Natural Sciences, Tampere University, Tampere, Finland
[b] Faculty of Mechanical, Maritime and Materials Engineering, Delft University of Technology, Netherlands

ARTICLE INFO

Keywords:
Industrial slags
Sintering
Reactivity
Selectivity
Material strength

ABSTRACT

Biomass Chemical Looping Gasification (BCLG) is a cost-effective and efficient alternative to conventional gasification. The selection of appropriate oxygen carriers (OCs) is crucial for stable BCLG performance. These OCs need to possess high reactivity, selectivity, material strength, and resistance to sintering. The study investigated various OC materials, including industrial wastes (copper, nickel slag, desulphurization, LD, and ladle slags), residential waste (sewage sludge ash), and natural ore (manganese). The evaluation of OCs focused on reactivity, H_2-selectivity, mechanical strength and sintering behaviour. Except for ladle slag, all OC samples exhibited favourable reactivity due to the presence of Fe- and Mn-oxides possessing high oxygen transport capacity (10–17.6%). Nickel slag, manganese ore, and desulphurisation slag displayed notable H_2-selectivity (8.7 to 10.4). It can be attributed to the presence of less-active (lattice) oxygen, limiting strong oxygen agents such as Fe_2O_3, Fe_3O_4, and Mn_2O_3. Moreover, desulphurization slag contained highly selective $Ca_2Fe_2O_5$, which falls within the partial oxidation zone of the Ellingham diagram. Furthermore, all OC samples exhibited desirable material strength (>20 MPa), suitable for fluidised bed reactors. However, nickel, LD, and ladle slags demonstrated limited sintering with sintering onset temperatures exceeding 963 °C. This limited sintering may be attributed to the absence of iron silicates, iron-bearing aluminium silicates, manganese silicates, and potassium that contributed to the low thermal stability observed in the remaining OCs. Altogether, nickel slag calcined at 1100 °C was identified as the most promising OC material with optimal reactivity, selectivity, material strength, and minimal sintering for BCLG. Overall, this study provides a detailed and scientific methodology for OC selection and can aid future OC development.

1. Introduction

Reducing anthropogenic CO_2 emissions is one of the major environmental concerns of this century, as the scientific community has established the link between the increase in atmospheric CO_2 levels and climate change. In this regard, it becomes imperative to adopt negative emissions technologies which can help remove CO_2 from the atmosphere and will be necessary for the future. One such negative emission technology is carbon capture and storage (CCS), and they function to stabilise atmospheric CO_2 emissions [1–3]. Among the CCS technologies, chemical looping processes (CLPs) have emerged as one of the most effective pathways to balance CO_2 emissions. Multiple scientific reports from IPCC, US Department of Energy and Energy Institute Europe have concluded that CLP is an effective and highly competitive CCS technology with the lowest cost of CO_2 reduction (≈$75/t$CO_2$ -avoided) [1,4,5]. BCLG is a CLP technology used for the gasification of solid fuels, including biogenic residues. BCLG is a dual-fluidised bed reactor system in which OC material (e.g., metal oxide) circulates between the two reactors to transport oxygen from combustion to the gasification reactor. Compared to conventional biomass gasification and combustion systems, BCLG could be 10–25% [1] more efficient and nearly 16% [6] more economical (levelised cost) for CO_2 mitigation.

The OC is the core of BCLG because they participate in all critical chemical reactions. Therefore, careful investigation and consideration of their physical and chemical properties are required for the selection of appropriate OCs. The most desirable characteristic of OC is reactivity which defines its ability to transfer oxygen from its matrix to biomass feed [1,7,8]. Furthermore, it is expected that OC will have high mechanical strength to withstand repeated cyclic operations and low sintering and agglomeration tendency during their interaction with

* Corresponding author.
E-mail addresses: avishek.goel@tuni.fi (A. Goel), chao.he@tuni.fi (C. He).

https://doi.org/10.1016/j.cej.2023.143948
Received 29 March 2023; Received in revised form 19 May 2023; Accepted 3 June 2023
Available online 5 June 2023

biomass feed and ash [1,8–14]. Additionally, the OC should be selective, environmentally benign and preferably low-cost to compensate for the process losses such as the separation of ash.

Even though BCLG is a promising technology, it still faces commercialisation issues due to some practical and technical impediments such as improvement of OCs (e.g., appropriate reactivity and selectivity, high attrition, sintering, agglomeration rates and cost and environmentally unfavourable) and reactor development (e.g., heat/mass integration and management). Among these, the development of OC is considered one of the key issues in advancing BCLG technology [1,8,15–21]. OCs development needs careful consideration of several properties and should be a good compromise between reactivity, selectivity, cost and mechanical strength. The selection of suitable OC for use in BCLG is critical and requires a comprehensive investigation of the aforementioned physical and chemical properties. Although there have been some investigations in the open literature regarding the application of manganese ore [7,22–26] and copper slag [27–31] in the BCLG process, the scientific literature reports limited studies focused using LD slag [32,33] and sewage sludge ash [34,35] in this process. While the studies have focused on the interaction of OC materials with biomass, there is a lack of in-depth examination of critical OC behaviour required for the BCLG process. More importantly, to the best of our knowledge, no studies are present which investigate utilisation of nickel slag, ladle slag and desulphurisation slag in BCLG process. Additionally, limited studies are present in the literature that discuss and investigate the selection/comparison of OC materials for the BCLG process [1,8,9,18,36–39]. Generally, these studies have compared pure metal oxide OCs, such as iron oxide, manganese oxide, nickel oxide, copper oxide, and cobalt oxide. Interestingly, none of the available studies provided an in-depth quantitative comparison of crucial parameters such as reactivity, selectivity, sintering behaviour (including sintering temperature and rate), and mechanical strength for low-cost materials. More importantly, the low-cost materials comprise complex mixtures of metal oxides, impurities, and inert compounds, exhibiting divergent behavior compared to pure metal oxide OCs in BCLG process.

Therefore, a systematic investigation that methodically compares the critical parameters for low-cost materials is essential to advance the development of OCs for the BCLG process. This study aims to methodically analyze and compare the performance of eight different low-cost materials for use in BCLG process. The study focuses on key properties, including reactivity, selectivity, sintering, and strength, to identify the most suitable material for BCLG. The OCs were analysed chemically to establish their compositions. Subsequently, the reactivity of the OCs was investigated, and a correlation was established between their compositions and reactivity. The H_2 production performance of the OCs was also compared to understand their selectivity performance. To assess the stability of the OCs, their mechanical strength and sintering behaviour were examined. This analysis aimed to understand the longevity of the OCs during the BCLG process. Finally, a comprehensive evaluation of all the considered OCs was conducted to select the most suitable material for the BCLG process. The evaluation considered all the aforementioned properties to determine the most appropriate material for the process.

2. Materials and methods

2.1. OC materials

Industrial waste, residential waste and natural ores have been considered potential OCs for the investigation. The use of such materials as OCs is preferred due to their abundant availability and low cost compared to synthetic OCs [9,18]. Furthermore, using waste materials such as industrial by-products and residential waste as OCs helps reduce environmental impact and corresponds to the concept of Circular Economy [40,41]. More importantly, unlike synthetic OCs, these materials can be directly used as OCs after simple treatments. The materials chosen for this study are discussed hereafter. The OC samples are shown in Fig. S1.

2.1.1. Copper slag

It is an industrial by-product of the copper smelting process, with its major component as fayalite (Fe_2SiO_4) [42,43]. It is estimated that approximately 2.2 tons of copper slag is generated for every ton of copper produced and nearly 24.6 million of it is produced annually worldwide [44,45]. Currently, copper slag is being dumped at landfill sites which waste precious land resources and causes secondary pollution. It holds promising potential as an OC candidate because fayalite can be decomposed into Fe_2O_3/Fe_3O_4 and SiO_2 through simple calcination treatment [44]. After that, the produced Fe_2O_3 and Fe_3O_4 can provide lattice oxygen for feed conversion during BCLG. The copper slag used for this study was provided by Boliden (Rönnskär unit) in Sweden.

2.1.2. Nickel slag

It is a by-product of the nickel smelter process and gets generated by natural cooling or water quenching of a melt formed during the smelting process of nickel. The nickel slag contains fayalite as a major component [11]. It is estimated that nearly 6–16 tons of nickel slag get generated for every ton of nickel produced [11]. Furthermore, nickel slag has a worldwide annual production of approximately 16–40 million tons and a meagre utilisation rate of 10%. Similar to copper slag, handling nickel slag is a challenge as it requires a large disposal area and causes secondary pollution [11]. The nickel slag was supplied by Boliden (Harjavalta unit) in Finland.

2.1.3. Linz-Donawitz (LD) slag

It is also called basic oxygen furnace or steel converter slag and gets generated as a by-product during pig iron conversion to steel in the blast furnace (see Fig. S2). Generally, 85–165 kg of LD slag gets generated for every ton of steel produced, thereby generating 165–320 million tons of LD slag worldwide annually [46]. LD slag majorly contains oxides of Ca, Si, Fe and Mn, which makes it attractive to be used as an OC [46,47]. For the study, LD slag was provided by SSAB Europe Oy.

2.1.4. Ladle slag

They are fine size particles produced in the ladle furnace during the refining stage of steel production (see Fig. S2) and mainly contain oxides of Ca. Typically, 20 kg of ladle slag is generated for every ton of steel. Therefore, it can be estimated that nearly 0.4 million tons per annum of ladle slag get produced worldwide. For the study, ladle slag was supplied by SSAB Europe Oy.

2.1.5. Desulphurisation (DS) slag

During steel production, the liquid iron is treated in a desulphuriser to meet the required steel sulphur specification (less than0.03%). In this process, sulphur in the slag is removed from the liquid iron and discharged as a waste, called DS slag (see Fig. S2) [48]. However, due to the lack of an effective DS slag utilisation method, it gets stockpiled in landfills and causes serious land and environmental pollution [49]. Approximately 20 kg of DS is generated per ton of steel produced. Therefore, we can approximate that 0.4 million tons of desulphurisation slag get generated worldwide annually. SSAB Europe Oy provided DS slag used in this work.

2.1.6. Manganese ore

Manganese is known to be the 12th most abundant element in the earth's crust, with total global reserves of approximately 1.5 billion tons [50]. The majority of the manganese produced is used for steel and iron production. Manganese ores typically comprise 30–60% of manganese in their oxide forms such as Mn_2O_3/Mn_3O_4 [51]. Therefore, it makes manganese ore a suitable candidate for use as OC. Manganese ore used for the study was sourced from Egypt.

2.1.7. Sewage sludge ash

It is a silty material generated as a by-product during the incineration of dewatered sewage sludge. Typically, during the incineration process, sewage sludge is reduced by 70 wt% to produce ash. Therefore, it can be estimated that sewage sludge ash has a generation potential of nearly 22.5–30 million tons per annum. However, the sludge incineration rates vary from country to country, with incineration rates as high as 100% in Japan, 90% in Germany, 60% in France, 26.7% in China and 20% in the United States [52,53]. More importantly, it is estimated that the sludge incineration practice will increase due to a 50–55% decrease in agricultural disposal and high landfilling prices [54]. Sewage sludge mainly contains iron, silica and alumina oxides, making it an interesting option for OC material. The sewage sludge used in this work was collected from the Tampere and Turku regions of Finland.

2.2. Preparation of OCs

2.2.1. Preparation of slags and ore

OC materials such as copper slag, nickel slag, LD slag, ladle slag, DS slag and manganese ore were dried at 105 ± 2 °C for 24 h to eliminate moisture. Next, the dried materials were calcined in a muffle furnace under atmospheric conditions, wherein the furnace temperature was increased from room temperature to the desired temperature (800 °C, 900 °C, 1000 °C, 1100 °C and 1200 °C) and then kept constant for 7200 s. Notably, the samples calcinated at 1200 °C were not considered in this study as they heavily agglomerated and got stuck to the crucible. Lastly, after natural cooling, the calcined samples were crushed and sieved to 400 μm mesh. Here it is noteworthy that the dried (@105 ± 2 °C) OC samples will be referred as ZD and the OC samples calcinated at 800 °C, 900 °C, 1000 °C and 1100 °C will be denoted as Z800, Z900, Z1000 and Z1100, respectively. Additionally, Z refers to CS, NS, LD, LAD, DS and MO indicate copper slag, nickel slag, LD slag, ladle slag, DS slag and manganese ore, respectively. Furthermore, industrially available iron oxide (Fe_2O_3) with a purity of 99% (particle size ≤ 5 μm) was used to compare the properties with other OC samples. Hereafter, it will be denoted as PIO.

2.2.2. Preparation of ashes

Sewage sludge ash samples were prepared according to the standard European ash preparation method (ASTM D 1102–84). Hereafter, sewage sludge ash samples from the Tampere and Turku region of Finland will be represented as SATM and SATR, respectively.

2.3. Characterisation of OCs

An X-ray fluorescence spectrometer (XRF, Thermo Scientific™ Niton XL3t GOLD) was used to determine the elemental composition of all the OC samples. Additionally, to study the crystal structure of the OCs, an X-ray diffractometer (XRD, Panalytical Empyrean X-Ray Diffractometer instrument) analysis was performed with Cu K_α radiation ($\lambda = 0.15406$ nm) at 40 kV with a current of 40 mA. The diffraction measurements were conducted over a 2θ range of 10° to 90° with a scanning speed of $0.05^\circ s^{-1}$.

2.4. Reactivity of OCs

Hydrogen-temperature program reduction (H_2-TPR) tests were conducted to investigate the reactivity of different OCs by examining and comparing their H_2 consumption behaviour. H_2-TPR tests were performed using a microreactor (CATLAB, Hiden Analytical, UK) and an online mass spectrometer system (QGA, Hiden Analytical, UK). In the tests, approximately 100 mg of OC sample was loaded onto a quartz tubular vertical flow reactor and reacted with H_2 (5 vol% H_2 balanced with helium and a total flow rate of $1.67x10^{-6}$ m^3/s). The OC samples were heated from room temperature to 950 °C at a heating rate of 10 °C/min and then maintained at a constant temperature of 950 °C for 1800 s.

2.5. H_2 production performance of OCs

The concept of methane reforming (partial oxidation of CH_4) was used to investigate and compare the affinity of different OCs for H_2-production. The experiments were performed using a microreactor system (CALTAB, Hiden Analytical, UK) and the produced gases such as CO, CO_2, H_2 and CH_4 were analysed using an online mass spectrometer (QGA, Hiden Analytical, UK). During each experiment, approximately 200 mg of OC sample was loaded onto a quartz tubular vertical flow reactor. The sample was heated from room temperature to 850 °C (heating rate: 10 °C/min) and then maintained at a constant temperature under an inert environment. At 850 °C, CH_4 (6 vol% balanced with He) was introduced with a total flow rate of 8.3x10-7 m^3/s for 3600 s.

2.6. Material strength of OCs

The determination of OC material strength was carried out using the granule bed compression test method, which was established by Järveläinen et al. [44]. This method involves compressing a granule bed to obtain an average particle strength, as opposed to testing individual particles. According to the authors, this method is suitable for determining the compressive strength of any brittle granular material with a size in the order of microns. In every test, a batch of 300 mg OC sample was uniaxially compressed with an Instron 5967 (Instron Industrial Products, UK) universal testing machine using a constant compression rate of 1.0 mm/min until an arbitrary limit of 10 kN. The test apparatus consisted of a bottom and top punch and a cylindrical die (ID: 11.61 mm), where the OC sample was poured and levelled by manual vibration (see Fig. S3). Additionally, the sliding surfaces were sprayed with silicone and wiped to eliminate wall friction.

2.7. Sintering behaviour of OCs

Dilatometric measurements of different OC materials were performed to investigate their sintering behaviour. The experiments were conducted using a DIL 402 Expedis horizontal pushrod dilatometer (Netzsch, Germany). The OC samples were separately uniaxially pressed into pellets by the Instron 5967 cylindrical punch setup described above, cut to the approximate cross-sectional size of 6 mm × 6 mm and then placed in the furnace chamber of the dilatometer. The samples were suspended between two alumina washers by a constant load of 200 mN applied by the pushrod. The measurements were carried out in a nitrogen purge gas flow of $6.67x10^{-7}$ m^3/s with temperature ranging from 25 °C to 1000 °C and heating rate of 10 °C/min. Notably, the experiment for the NS1100 sample was performed using an aluminium nitride powder sleeve due to lack of mechanical integrity for normal measurement.

3. Results and discussion

3.1. Chemical composition analysis

XRF analysis was conducted to investigate and compare the elemental composition of different OC samples. The iron content of all the OC samples is compared and presented in Fig. S4. The detailed elemental composition of all the OC samples is presented in Fig. S5 for brevity. It can be said that the concentration of iron is in the following order: nickel slag (~40%) > copper slag (~35%) ≈ SATM (~34%) > SATR (~27%) > manganese ore (~11%) ≈ LD slag (~11%) > desulphurisation slag (7.5%) > ladle slag (~1%). Similar results were presented by several other studies [27,30–32,55,56]. Furthermore, the change in iron concentration of each sample varies mildly with respect to their calcination temperatures. However, the change can be attributed to the release of volatiles during calcination. In the case of manganese ore, it is evident that the manganese concentration is the highest, with nearly 50% in value. Similar composition results were presented by

Arjmand et al. [57].

XRD patterns of the dried and calcined (at different temperatures) nickel slag are presented in Fig. 1a. Copper slag samples displayed a similar behaviour to nickel slag, and therefore, it is shown in Fig. S6. It is observed that NSD majorly contains fayalite (Fe_2SiO_4) along with smaller concentrations of SiO_2. However, with the calcination of the NSD sample, the fayalite phase disappeared, and three new phases (Fe_2O_3, Fe_3O_4 and SiO_2) appeared. The intensity of the Fe_2O_3 phase gradually increased with the increase in calcination temperature; the highest intensity was observed at 1100 °C. This trend can be attributed to reaction Eqs (1) and (2). Additionally, it is well understood that at calcination temperature below 1100 °C, reaction Eq. (1) dominates, indicating higher concentrations of Fe_2O_3 and SiO_2 [27]. Next, the XRD analysis of all LD slag samples is presented in Fig. 1b. Similar XRD behaviour was presented by Hildor et al. [58]. Ladle slag samples exhibited similar behaviour to LD slag samples, and hence it is shown in Fig. S7. It is observed that the dried sample of LD slag contains complex compounds along with iron oxide, calcium and silica. However, the complex compounds majorly decomposed into CaO at higher calcination temperatures. More importantly, it is observed that LD1100 and LAD1100 majorly contain calcium in their oxidised states such as CaO and calcium aluminium oxide/silicate, respectively. Next, the XRD analysis of all manganese ore samples is presented in Fig. 1c. Similar to nickel and LD slag samples, the manganese iron oxide silicate is concentrated in the MOD sample and decomposes to simpler forms such as Mn_2O_3, Mn_3O_4, and SiO_2. Similar XRD behaviour of manganese ore was reported by Arjmand et al. [57]. Comparing the XRD patterns, we can say that MO900 has the highest concentration of Mn_2O_3, and its concentration decreased with an increase in calcination temperatures. For desulphurisation slag, the complex oxide compounds of Ca, Si and Fe present in DSD decomposed at higher calcination temperatures to majorly form CaO, SiO_2, and $Ca_2Fe_2O_5$ (see Fig. S8). Interestingly, it was observed that DS1100 gradually changed its composition despite being stored in a dry airtight container at NTP conditions. Analysing the sample after nearly five months demonstrated that an additional phase of $Ca_2Fe_2O_5$ formed alongside the already existing CaO phase. Fig. 1d displays the XRD patterns of SATM. Xu et al. [34] reported similar XRD behaviour for sludge ash. Additionally, similar patterns for SATR were also observed; therefore, XRD analysis of SATR is presented Fig. S9 for brevity. Analysing the XRD patterns, it can be mentioned that Fe_2O_3, Fe_3O_4 and SiO_2 are present in significant concentrations.

Integrating the results from XRF and XRD of different OC samples, it can be concluded that 34.3% and 39.4% iron present in CS1100 and NS1100 is majorly concentrated as Fe_2O_3 and Fe_3O_4. Furthermore, the 41.9% and 33.5% calcium available in LD1100 and LAD1100 are mainly present in CaO and calcium aluminium oxide/silicate, respectively. Moreover, 51% calcium and 6.1% iron are majorly present in the form of CaO and $Ca_2Fe_2O_5$ in DS1100. Additionally, 50.9% of manganese available in MO900 is mainly present in Mn_2O_3 form. Finally, 34.7% and 26.7% of the iron in SATM and SATR are mainly concentrated in Fe_2O_3

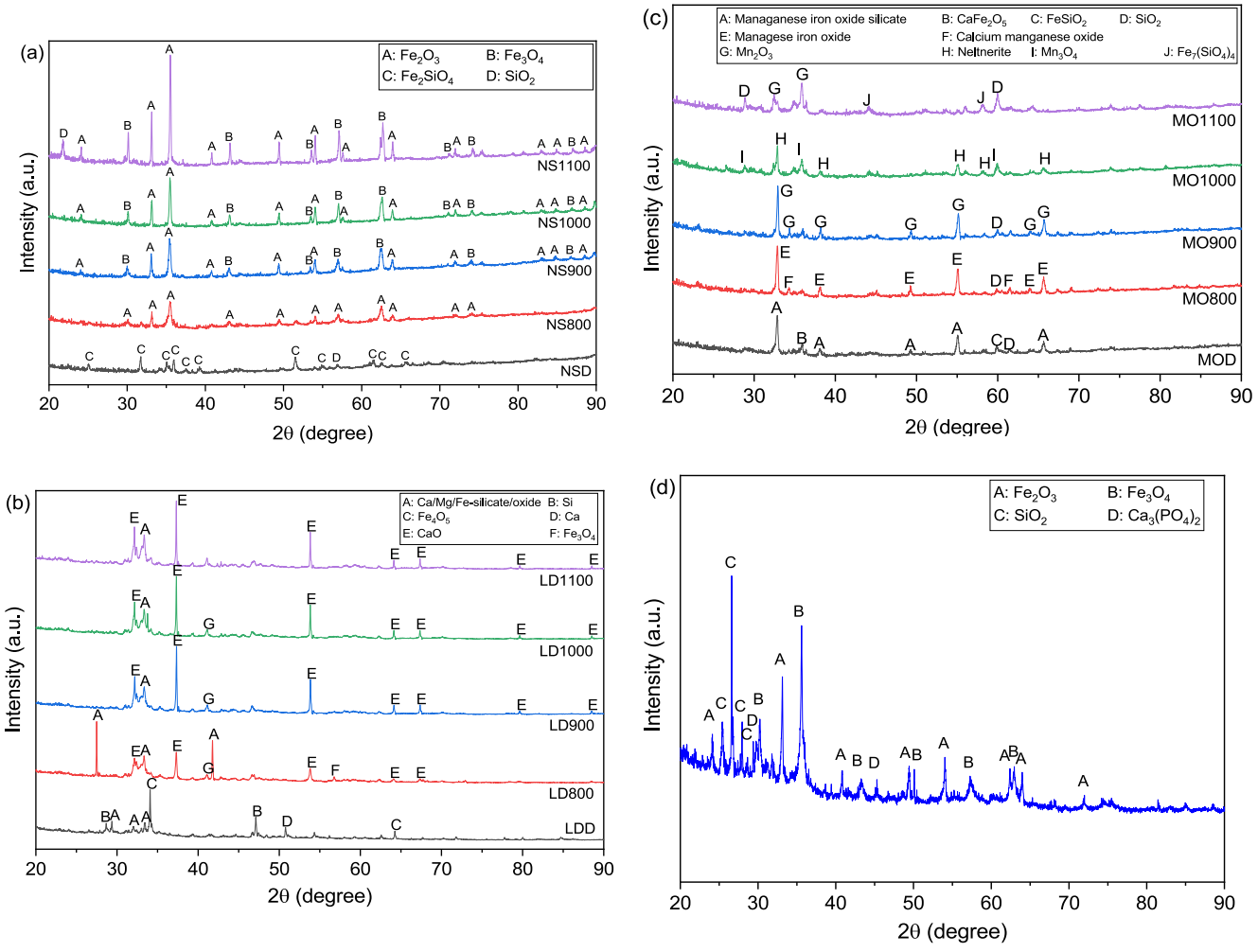

Fig. 1. XRD analysis of (a) nickel slag, (b) LD slag, (c) manganese ore and (d) SATM samples.

and Fe_3O_4 forms. To this end, we can infer that CS1100, NS1100, MO900, DS1100, SATM and SATR hold promising potential to become suitable OC for BCLG process.

$$2Fe_2SiO_4 + O_2 \rightarrow 2Fe_2O_3 + 2SiO_2 \quad (1)$$

$$6Fe_2O_3 \rightarrow 4Fe_3O_4 + O_2 \quad (2)$$

3.2. Relationship between chemical composition and reactivity

H_2-TPR experiments were carried out to investigate and compare the reactivities of different OC samples, and the results are presented in Fig. 2. Generally, a large area under the curve indicates a higher reactivity as the oxidisability of the OC sample is mirrored by its reduction area. In Fig. 2, the reduction behaviour of PIO, CS1100, NS1100, SATM and SATR is similar with three reduction zones, implying a stepwise reduction. The H_2-TPR curve of the CS1100 sample is very similar to the results presented by Deng et al. [27] in their study to evaluate copper slag as OC. The first reduction zones correspond to the reduction of hematite to magnetite ($Fe_2O_3 \rightarrow Fe_3O_4$) and lie between a temperature range of 300–450 °C. Additionally, the second and third reduction zones (between the temperature range of 450–950 °C) reflect the transformation of magnetite to metallic iron with intermediate as wustite $Fe_3O_4 \rightarrow FeO \rightarrow Fe$ [59–61,61–63]. However, the second and third reduction zones for PIO, CS1100 and NS1100 samples are characterised by a broad region wherein the zones are severally overlapped. This could be attributed to the non-uniform distribution of iron oxide particles and similar reduction mechanisms of Fe_3O_4 and FeO [61,64]. The simultaneous reduction of larger Fe_3O_4 particles and FeO reduction could lead to an unclear transition between the second and third reduction zones. The H_2-consumption for the LD1100 sample was observed in a broad temperature range of 300–950 °C (see Fig. 2). The behaviour is similar to the LD slag reduction study by Guo et al. [65]. Combining the LD slag XRD pattern (see Fig. 1b), we can say that the H_2-consumption is mainly due to the presence of iron-oxide/silicate compound. Next, we examined the H_2 reduction behaviour of the DS1100 sample and observed a sharp peak maximising at 748 °C (see Fig. 2). We can infer that the H_2-reduction is due to $Ca_2Fe_2O_5$. Next, the H_2-consumption pattern for MO900 was studied, and two reduction peaks at 714 °C and 840 °C were detected (see Fig. 2). The two-peak reduction behaviour was similar to the pure Mn_2O_3 H_2-reduction pattern [66]. The reduction peaks can be ascribed to the transformation of Mn_2O_3 into the Mn_3O_4 phase and Mn_3O_4 into the MnO phase, respectively. Lastly, no considerable H_2-consumption behaviour was observed for the LAD1100 sample (see Fig. 2).

Post investigation of H_2-reduction behaviours of multiple OC samples, we calculated their H_2 consumption using the fact that the intensity signal is linearly related to the H_2-concentration [59]. The H_2 consumption values for different OC samples are shown in Fig. 3. The H_2 consumption values were determined for a 100 g OC sample. Here, the error bars represent the H_2 calibration errors. Furthermore, the reactivities of the OC samples are in the following order: CS1100 ≈ NS1100 ≈ MO900 > SATM ≈ SATR ≈ DS1100 > LD1100 > LAD1100. As expected, PIO comprising 99% pure Fe_2O_3 had the maximum H_2 consumption and, therefore highest reactivity. Additionally, the results indicate that the H_2 consumption of CS1100, NS1100, SATM and SATR lies in the range of 2.5–3.1x10^{-4} mol. This can be attributed to the presence of Fe_2O_3 and Fe_3O_4 in the OCs, which have a high oxygen transport capacity of 10% [1,8]. The slightly higher H_2 consumption of CS1100 compared to NS1100 despite having 5% lower Fe content is

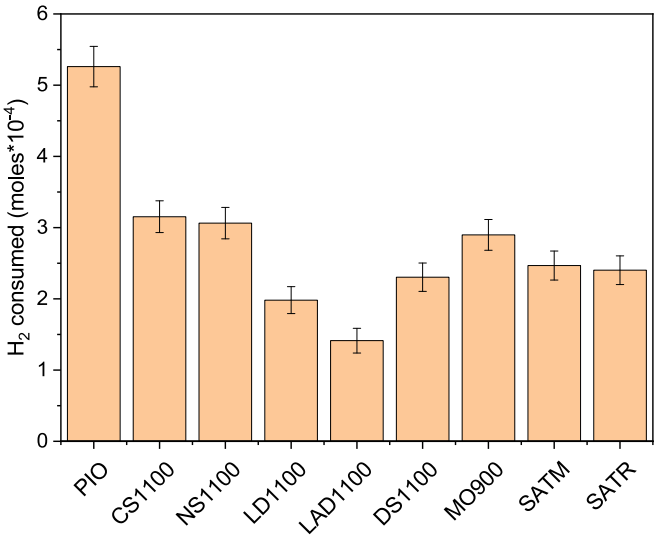

Fig. 3. H_2 consumption values (per 100 g sample) of OCs.

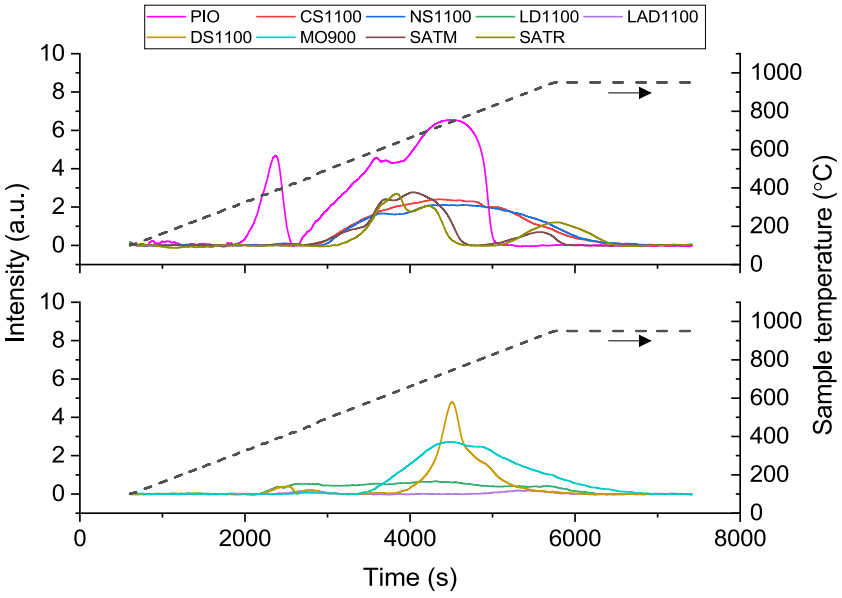

Fig. 2. H_2-TPR profile of different OC samples.

attributed to the relatively higher concentration of Fe_2O_3 in CS1100. This difference in Fe_2O_3 concentration can be observed from the X-ray diffraction (XRD) analyses presented in Fig. S6 and Fig. 1a. The lower H_2 consumption of SATM and SATR than CS1100 or NS1100 can be explained due to the lower Fe content in these OCs. MO900 had a high H_2 consumption value (similar to NS1100 and CS1100) due to the high oxygen transport capacity of 10% for Mn_2O_3/MnO [8] and the presence of nearly 50% manganese in MO900. DS1100 had a reasonable reactivity similar to SATR and SATM due to the presence of $Ca_2Fe_2O_5$, which has a high oxygen transport capacity of 17.6% for $Ca_2Fe_2O_5$/CaO + Fe [19,67]. However, limited H_2 consumption may be attributed to the low concentration of $Ca_2Fe_2O_5$ in DS1100 which can be observed from the XRD analysis shown in Fig. S8. Furthermore, LD1100 had a low H_2 consumption value, reflecting its low oxygen transport capacity of approximately 1% due to the presence of calcium-silicate-metal oxide [32,58,68]. Finally, LAD1100 had the lowest H_2 consumption value due to the dominant calcium aluminium silicate, as seen in the XRD analysis in Fig. S7.

3.3. Comparative study on H_2-production performance

After comparing the reactivities of multiple OC samples, it was imperative to understand their selectivity towards H_2 (or syngas) generation. To investigate this, we examined the oxidation behaviour of CH_4 (partial or complete) by introducing CH_4 over different OCs. The produced gas intensity signals post CH_4 cracking are presented in Fig. 4. Here, it is noteworthy that the CH_4 cracking behaviour was studied at a single temperature of 850 °C and not against a gradual temperature increase to imitate real reactor conditions. To better under the performance, we quantified the OC's H_2-production performance (HPP) by normalising the area under H_2-production intensity signals against a standard reference material PIO, and the results are shown in Table 1. From Fig. 4, it can be understood that methane gas got cracked immediately upon introduction and converted into CO_2 (rather than H_2 and CO) for OCs such as CS1100, SATM, SATR, LD1100 and LAD1100. It is reflected in their HPP values which lie between 0.7 and 2.6. This can be attributed to the presence of more surface (active) oxygen than lattice oxygen [69,70]. Additionally, Fe_2O_3 and Fe_3O_4, present in CS1100, SATM, and SATR, lie in the combustion zone of Ellingham, making it a strong oxidizing agent that can completely oxidize the fuel [8]. Furthermore, DS1100 and MO900 displayed high HPP values greater than 10, indicating a higher presence of less-active oxygen (lattice oxygen) [69,70]. It is also reflected in their H_2 production intensity signals, where a broad valley of CH_4 consumption is observed, indicating higher

Table 1
H_2-production performance of different OC samples.

OC	H_2-production performance
PIO	1.0
CS1100	2.6
NS1100	8.7
LD1100	0.9
LAD1100	1.0
DS1100	10.0
MO900	10.4
SATM	0.9
SATR	0.7

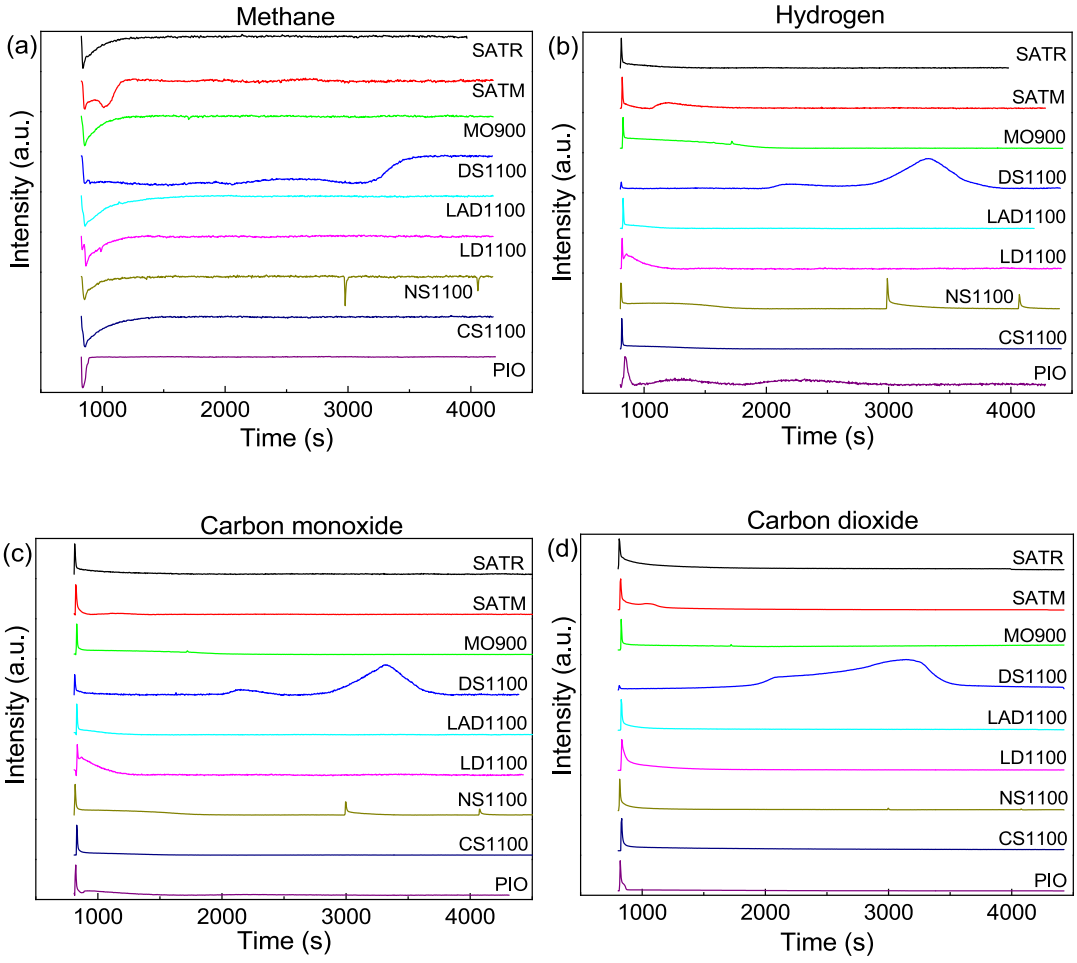

Fig. 4. Intensity signal of (a) CH_4, (b) H_2, (c) CO and (d) CO_2 post methane cracking.

selectivity towards partial oxidation of CH_4. Similar behaviour was observed by Bhavsar et al. [71], wherein syngas selectivity was higher than 70%. Additionally, Zhang et al. [19] and Wang et al. [67] confirmed the high selectivity of $Ca_2Fe_2O_5$ towards H_2 production. The authors mentioned that higher H_2 production can be attributed to the active sites provided by $Ca_2Fe_2O_5$ and its presence in partial oxidation zone of the Ellingham diagram. In the case of NS1100, the HPP value was calculated as 8.7 and complemented gradual CH_4-consumption and H_2-production emphasised by three peaks. Additionally, the strong oxidizing properties of Fe_2O_3 and Fe_3O_4, located in the combustion zone of the Ellingham diagram, are contradicted by a high HPP value which indicates the presence of less active (lattice) oxygen. Therefore, it can be inferred that, similar to DS1100 and MO900, the concentration of lattice oxygen dominated surface oxygen for NS1100.

3.4. Stability of OCs

Examining the physical properties of OCs are equally important as chemical ones, therefore OC materials were investigated for their mechanical strength and sintering behaviour.

3.4.1. Evaluation of mechanical strength

The mechanical strength of different OC materials was determined using their respective compressive strength curve consisting of measured relative density vs logarithmic pressure values. The compression curve shown in Fig. 5a is divided into three stages: (i) in stage 1, the granules elastically deform, pack and rearrange themselves, thereby increasing the relative density; (ii) in stage 2, the granule's compressive strength increases and they start fracturing; and (iii) in stage 3, the fractured granules start rearranging themselves similar to stage 1. As shown in Fig. 5a, the average compressive strength value lies in the second stage, where the compression curve forms the steepest contour. At this location, the relative density of the granules increases most rapidly with just a slight increase in pressure. This indicates the pivoting point where the granule bed starts yielding and can be interpreted as the fracture point for fragile materials. Typically, the average compression strength value is determined by locating the intercept formed by extrapolating the linear regressions from stages 1 and 3. Notably, the first regression line was anchored at 0.1 MPa to reduce experimental noise. At the same time, the second regression line was anchored at the maximum pressure point.

Post determination, the average compressive strength values of different OC materials were compared and are presented in Fig. 5b. It is noteworthy that the average compressive strength values of PIO, SATM and SATR could not be determined as the samples were in dust form (particle size less than 10 μm). Additionally, the experiments were repeated thrice, and the standard deviation was within the acceptable error range. Fig. 5b shows that the compressive strength of MO900 was the highest, followed by LAD1100 > CS1100 > NS1100 > LD1100 > DS1100. Furthermore, the compressive strength values of MO900 and CS1100 were similar to the results presented by Arjmand et al. [57] and Maniraman et al. [51] for manganese ore and copper slag, respectively. Interestingly, an OC material is prone to breaking and blown out of the reactor when its compressive strength is less than 10 MPa [72]. However, Rydén et al. [73] conducted an extensive study on mechanical strength using multiple OCs and concluded that OCs with a mechanical strength of more than 20 MPa are likely to perform better by achieving sufficient resistance towards attrition. In this regard, it can be mentioned that all the considered OCs (except PIO, SATM and SATR) were found suitable for BCLG application.

3.4.2. Study of sintering behaviour

Bed defluidisation occurs when the particles bond due to sintering cannot be broken apart by the particle's kinetic energy [40,74,75]. The sintering onset temperature, T_{sin} (also referred to as defluidisation temperature), is the temperature at which the surface of the particle

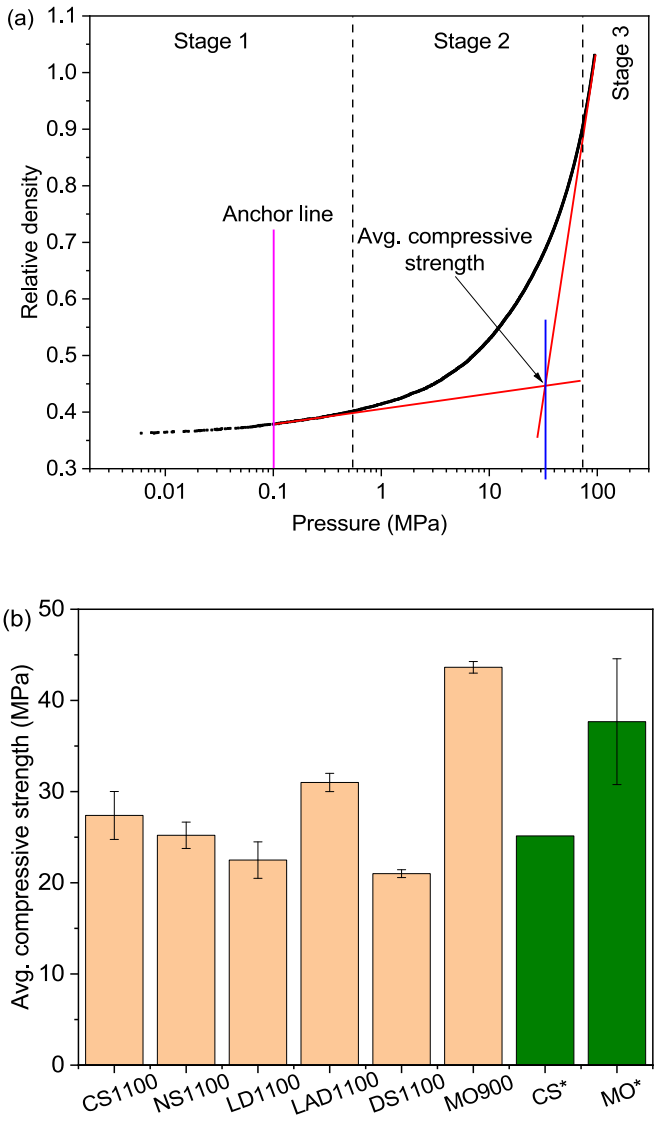

Fig. 5. (a) Determination of average compressive strength of a granule bed and (b) comparison of average compressive strength of different OC materials. The material strength results of copper slag (CS) and manganese ore (MO) are marked with an asterisk (*). These results were derived from studies by Arjmand et al. [57] and Maniraman et al. [51].

begins to soften and become cohesive. This temperature is lower than the melting temperature of the particle and was first demonstrated by Gluckman et al. [76]. The authors showed that when particles are fluidized at temperatures higher than T_{sin}, the minimum fluidisation velocity is no longer determined only by the balance of gravity, buoyant and drag forces. Interparticle cohesiveness and particle kinetic energy must also be taken into account. Additionally, when the temperature is higher than T_{sin}, the gas velocity required to counteract the cohesive forces is higher than the minimum fluidisation velocity, leading to particle agglomeration. Therefore, it becomes vital to determine the T_{sin} of the particles and predict their defluidisation behaviour. In this study, we investigated the sintering behaviour of various OC materials by determining their T_{sin} and degree of sintering through dilatometry analysis. The results are presented in Fig. 6. It can be observed that the OC materials first dilated upon heating. It is attributed to the thermal expansion of the solid material and is a bulk property of the particle. Upon further heating, the powder sample started densifying, leading to a small contraction. At this temperature, there is just enough contraction to balance the thermal expansion, and it is characterised by a plateau

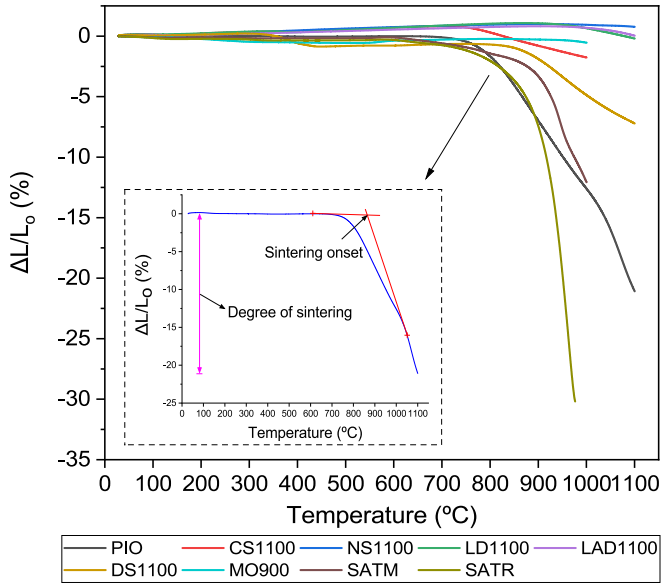

Fig. 6. Sintering behaviour of different OC samples.

region. As the sample is heated further, the contraction rate dominates the thermal expansion rate, resulting in significant contraction and sintering. This temperature is marked as the sintering onset point (T_{sin}) in Fig. 6, and the particles start to agglomerate after this temperature. Here it is noteworthy that the determination of T_{sin} is an inherent feature of the analysis software provided with the Netzsch DIL 402 Expedis dilatometer. The degree of sintering refers to the amount of contraction and is defined as the contraction length of the OC pellet per unit initial length ($\Delta L/L_0$). The value of ΔL is determined between the sintering onset temperature and 1000 °C. In the case of DS1100, a slight contraction is observed around 350 °C, possibly due to a phase change of the sample. In Table 2, we compared the T_{sin} and degree of contraction (until 1000 °C) of all the OC samples. It can be said that LAD1100 has the T_{sin}, followed by LD1100 > NS1100 > SATR > SATM > PIO ≈ DS1100 > MO900 > CS1100. Furthermore, LAD1100, LD1100, NS1100, CS1100 and MO900 sintered the least with less than 2% degree of sintering. DS1100, SAM and PIO also sintered moderately with a 5–13% degree of sintering. Interestingly, SATR sintered heavily with nearly 29% degree of sintering. Table 2 presents that OC samples such as PIO, LD1100, DS1100, CS1100, NS1100, SATM and SATR have T_{sin} around 750–950 °C. It may be attributed to the presence of iron oxides and iron silicates, which have low thermal stability and may start to melt at a relatively lower temperature [77–82]. In particular, iron oxides can react with quartz and form lower melting point (900–1000 °C) eutectics [82]. Iron oxides can also react with clay minerals and generate iron-bearing aluminium silicates with low melting points that contribute to severe sintering [83]. More importantly, pure iron oxides have low Tamman temperatures of around 800 °C [84,85] and suffer serious sintering [86–89]. Furthermore, the presence of potassium in CS1100, SATM and SATR promoted additional sintering. Schmid et al. [89] indicated similar sintering onset temperatures (around 900 °C) for sewage sludge ashes. For MO900, the T_{sin} can be ascribed to the formation of manganese silicates with low melting points due to the interaction of SiO_2 and Mn_2O_3 [26]. Typically, the temperatures in fuel and air reactors range between 800 and 900 °C and 900–1000 °C, respectively. In this regard, it can be concluded that LAD1100, LD1100 and NS1100 could be suitable for the BCLG process.

Table 2
Sintering onset temperatures and degree of sintering of different OC samples.

OC	Sintering onset temperature (°C)	Degree of sintering (%) (≤1000 °C)
PIO	869.4	12.65
CS1100	759.5	1.76
NS1100	963.0	0.01
LD1100	965.7	0.01
LAD1100	1034.5	0
DS1100	869.2	4.89
MO900	826.4	0.54
SATM	907.9	12.07
SATR	911.3	28.84

3.5. Comprehensive evaluation of OCs

As discussed at the beginning of the study, low-cost and readily available OC materials were chosen for this investigation concerning the economic feasibility of BCLG process. The materials were treated using simple calcination and standard ash preparation method. The detailed material characterisation was carried out for all the materials; consequently, CS1100, NS1100, LD1100, LAD1100, DS1100, MO900, SATM and SATR were selected for further investigation. The most important parameters, such as reactivity, HPP, material strength and sintering behaviour, were studied during the investigation. Therefore, the results from these investigations needed to be systemically integrated to comprehensively evaluate the most suitable OC for BCLG process. The outcomes are presented in Fig. 7.

Although CS1100 hold good reactivity due to considerable H_2 consumption and desired material strength, it is expected that using CS1100 as OC may lead to bed defluidisation due to its very low sintering onset temperature. Furthermore, MO900 has high reactivity, exceptionally good HPP and the highest material strength; however, similar to CS1100, its sintering onset temperature is low and can lead to bed agglomeration and consequently defluidisation. Moreover, LAD1100 has the highest sintering onset temperature and a desirable material strength but holds a poor reactivity which is also reflected in the material characterisation. Despite having reasonable reactivity, good HPP, and desirable material strength, DS1100 has a low sintering onset temperature and may not be suitable as an OC bed material. Next, the sewage sludge ashes (SATM and SATR) have an extremely high degree of sintering and an undesirably low sintering onset temperature. Additionally, the particle size of the ashes is less than 10 μm and are likely to be eroded during fluidisation, making them unsuitable for BCLG reactors. The remaining OCs such as NS1100 and LD1100 have high sintering onset temperatures (~960 °C), negligible degree of sintering and desirable material strengths of more than 20 MPa. However, NS1100 has higher reactivity and significantly greater HPP than LD1100. More importantly, comparing the performance against PIO, it is evident that NS1100 has a higher sintering onset temperature and a lower rate of sintering. To this end, we can conclude that nickel slag calcined at a temperature of 1100 °C is considered the most suitable OC among all the evaluated OC materials.

In Fig. 7h, optimal reactivity of NS1100 with a high H_2 consumption of 3.1 mol/100 g sample was presented, which could be attributed to the nearly 40% Fe content in the form of Fe_2O_3 or Fe_3O_4 and high oxygen transport capacity of 10% for Fe_2O_3/FeO. Furthermore, NS1100 exhibited adequate material strength of 25 MPa, which exceeded the required strength of 20 MPa for fluidised bed reactors, and was consistent with previous observations regarding Fe-OC possessing high mechanical strength and resistance to attrition [1,8]. Additionally, NS1100 demonstrated high selectivity towards H_2 production with an HPP of 8.7, as evidenced by the gradual consumption of H_2 and CH_4 over an extended period during H_2-TPR and CH_4-reforming, respectively. Lastly, NS1100 exhibited an acceptable onset sintering temperature of 963 °C and a minimal degree of sintering (0.01% until 1000 °C), which was complemented by high melting points of Fe-oxides in the range of 1300–1600 °C [1]. The results of this study will prove advantageous in selecting suitable OC materials for conducting BCLG experiments in fluidized bed reactors. It should be noted that the BCLG investigation of

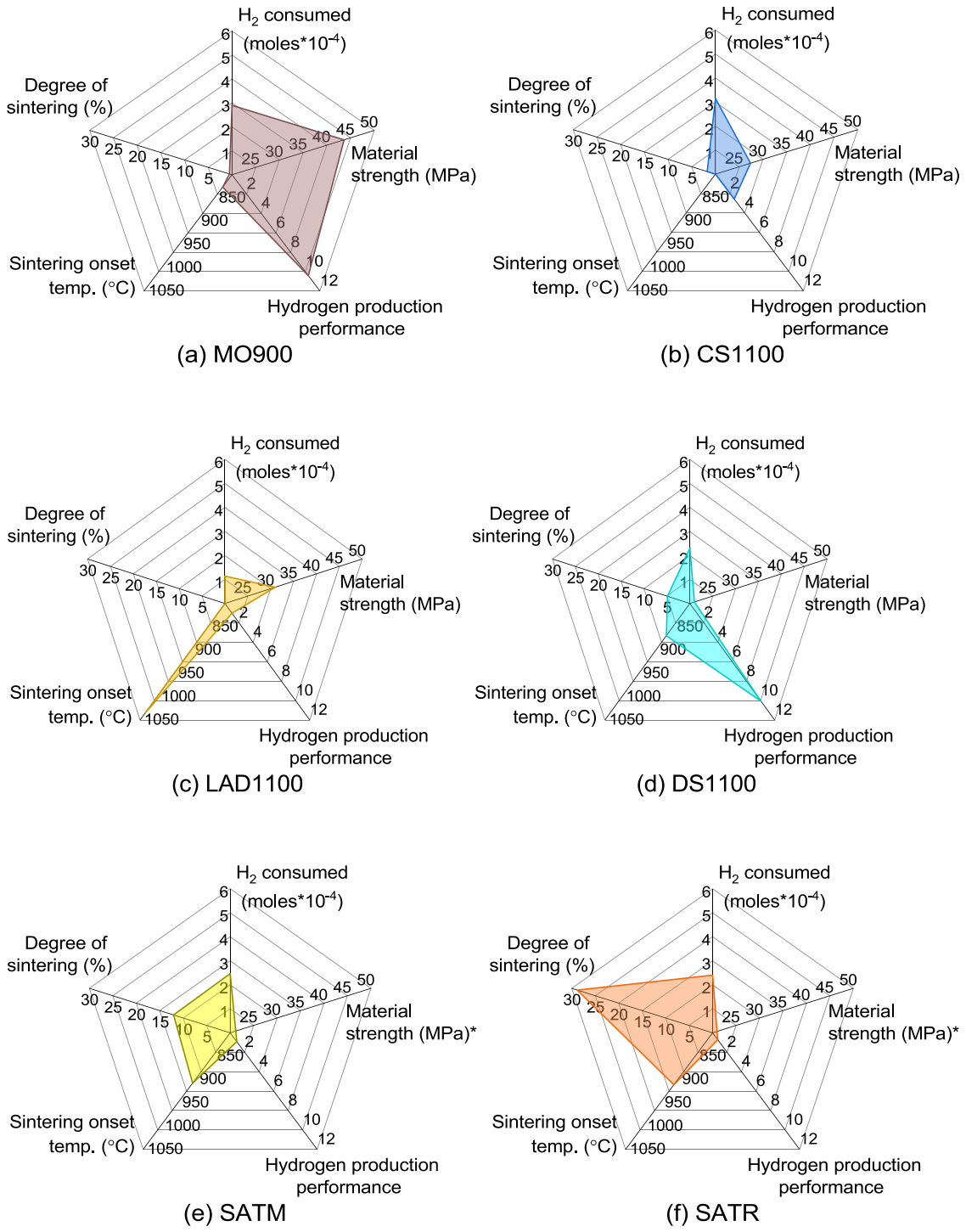

Fig. 7. Overall analysis of (a) MO900, (b) CS1100, (c) LAD1100, (d) DS1100, (e) SATM, (f) SATR, (g) LD1100, (h) NS1100 and (i) PIO OC samples. The mechanical strength of SATM, SATR and PIO OC samples could not be determined and hence marked with an asterisk (*) in the figure.

selected OC using fluidised bed reactors is ongoing and the outcomes will be disseminated in a separate research article.

4. Conclusion

In this work, the physical and chemical properties of various low-cost materials were comprehensively characterised and evaluated towards the selection of cost-effective OC for an efficient BCLG process. Eight samples were initially screened based on material characterization, followed by evaluation of reactivity, selectivity, material strength, and sintering behaviour. Except for LAD1100, the OC materials exhibited reasonable reactivities, with the consumption of more than 2.0 mol of H_2 per 100 g sample. This reactivity was attributed to the presence of Fe- and Mn-oxides, which possess high oxygen transport capacity. Comparing the H_2 production performance using PIO as a standard reference material, NS1100, DS1100, and MO900 demonstrated higher performance (8.7–10.4), while CS1100, LD1100, LAD1100, SATM, and SATR showed lower performance (0.7–2.6). The high selectivity

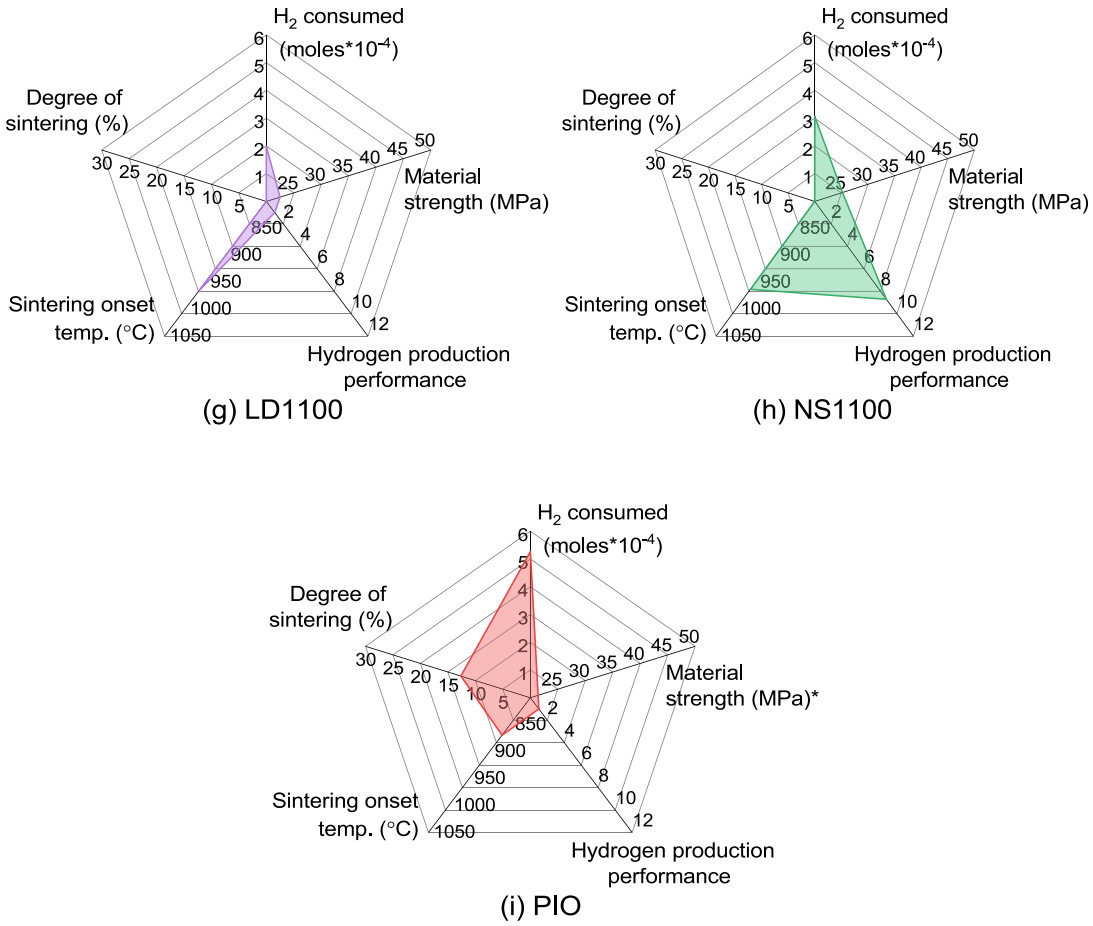

Fig. 7. (*continued*).

observed can be attributed to the presence of less active (lattice) oxygen in strong oxidising agents such as Fe_2O_3, Fe_3O_4, and Mn_2O_3, as well as the highly selective $Ca_2Fe_2O_5$ compound. All OCs possessed desirable material strengths exceeding 20 MPa, suitable for fluidized bed reactors. Among them, only LAD1100, LD1100, and NS1100 demonstrated adequate sintering onset temperatures (963–1034 °C) with negligible degrees of sintering up to 1000 °C (≤0.01%). This limited sintering was attributed to the absence of less thermally stable compounds like iron silicates, iron-bearing aluminium silicates, manganese silicates, and potassium, which contributed to the lower thermal stability of the remaining OCs. Based on a comprehensive evaluation, NS1100 emerged as the most suitable OC for the BCLG process. NS1100 exhibited reasonable reactivity due to the presence of Fe_2O_3 and Fe_3O_4 that have high oxygen transport capacity. Additionally, the presence of less active (lattice) oxygen in Fe_2O_3 and Fe_3O_4 contributed to its high H_2 selectivity. Furthermore, NS1100 possessed a desirable material strength of 25 MPa and an acceptable onset sintering temperature of 963 °C. The limited sintering behaviour was complemented by the high melting point of Fe-oxides.

Declaration of Competing Interest

The authors declare the following financial interests/personal relationships which may be considered as potential competing interests: Chao He reports financial support was provided by Academy of Finland.

Data availability

Data will be made available on request.

Acknowledgement

This work is supported by Tampere University, the Academy Research Fellowship and its related research project funded by Academy of Finland (decision numbers: 341052, 346578). The authors would like to acknowledge the support of Pasi Arvela (TAMK), Madan Patnamsetty (TAU) and Leo Hyvärinen (TAU) during the characterisation of materials. The authors would also like to acknowledge Boliden (for providing copper, nickel and desulphurisation slag), SSAB (for providing LD and ladle slag), Gasum Oy and Dr. Daofeng Mei from Chalmers University of Technology (for providing manganese ore).

Appendix A. Supplementary data

Supplementary data to this article can be found online at https://doi.org/10.1016/j.cej.2023.143948.

References

[1] A. Goel, E.M. Moghaddam, W. Liu, C. He, J. Konttinen, Biomass chemical looping gasification for high-quality syngas: a critical review and technological outlooks, Energy Convers. Manag. 268 (2022), 116020.
[2] D.L. Sanchez, J.H. Nelson, J. Johnston, A. Mileva, D.M. Kammen, Biomass enables the transition to a carbon-negative power system across western North America, Nat. Clim. Change. 5 (2015) 230–234.
[3] P. Lamers, R. Hoefnagels, M. Junginger, C. Hamelinck, A. Faaij, Global solid biomass trade for energy by 2020: an assessment of potential import streams and supply costs to North-West Europe under different sustainability constraints, Gcb Bioenergy. 7 (2015) 618–634.
[4] A. Bhave, R.H.S. Taylor, P. Fennell, W.R. Livingston, N. Shah, N.M. Dowell, J. Dennis, M. Kraft, M. Pourkashanian, M. Insa, J. Jones, N. Burdett, A. Bauen, C. Beal, A. Smallbone, J. Akroyd, Screening and techno-economic assessment of

biomass-based power generation with CCS technologies to meet 2050 CO2 targets, Appl. Energy. 190 (2017) 481–489.
[5] L.-S. Fan, L. Zeng, W. Wang, S. Luo, Chemical looping processes for CO2 capture and carbonaceous fuel conversion–prospect and opportunity, Energy Environ. Sci. 5 (2012) 7254–7280.
[6] B. Parkinson, P. Balcombe, J.F. Speirs, A.D. Hawkes, K. Hellgardt, Levelized cost of CO2 mitigation from hydrogen production routes, Energy Environ. Sci. 12 (1) (2019) 19–40.
[7] A. Hedayati, A.H. Soleimanisalim, C.J. Linderholm, T. Mattisson, A. Lyngfelt, Experimental evaluation of manganese ores for chemical looping conversion of synthetic biomass volatiles in a 300 W reactor system, J. Environ. Chem. Eng. 9 (2021), 105112.
[8] N.M. Nguyen, F. Alobaid, P. Dieringer, B. Epple, Biomass-based chemical looping gasification: overview and recent developments, Appl. Sci. 11 (2021) 7069.
[9] Y. Lin, H. Wang, Y. Wang, R. Huo, Z. Huang, M. Liu, G. Wei, Z. Zhao, H. Li, Y. Fang, Review of biomass chemical looping gasification in China, Energy Fuels. 34 (7) (2020) 7847–7862.
[10] X. Tian, P. Niu, Y. Ma, H. Zhao, Chemical-looping gasification of biomass: part II Tar yields and distributions, Biomass Bioenergy. 108 (2018) 178–189.
[11] Y. Wu, Y. Liao, G. Liu, X. Ma, Syngas production by chemical looping gasification of biomass with steam and CaO additive, Int. J. Hydrog. Energy. 43 (42) (2018) 19375–19383.
[12] Z. Huang, F. He, H. Zhu, D. Chen, K. Zhao, G. Wei, Y. Feng, A. Zheng, Z. Zhao, H. Li, Thermodynamic analysis and thermogravimetric investigation on chemical looping gasification of biomass char under different atmospheres with Fe2O3 oxygen carrier, Appl. Energy. 157 (2015) 546–553.
[13] C. Dueso, C. Thompson, I. Metcalfe, High-stability, high-capacity oxygen carriers: iron oxide-perovskite composite materials for hydrogen production by chemical looping, Appl. Energy. 157 (2015) 382–390.
[14] L.F. de Diego, F. García-Labiano, J. Adánez, P. Gayán, A. Abad, B.M. Corbella, J. María Palacios, Development of Cu-based oxygen carriers for chemical-looping combustion, Fuel. 83 (13) (2004) 1749–1757.
[15] T. Mendiara, F. García-Labiano, A. Abad, P. Gayán, L. De Diego, M. Izquierdo, J. Adánez, Negative CO2 emissions through the use of biofuels in chemical looping technology: a review, Appl. Energy. 232 (2018) 657–684.
[16] X. Zhao, H. Zhou, V.S. Sikarwar, M. Zhao, A.-H. Park, P.S. Fennell, L. Shen, L.-S. Fan, Biomass-based chemical looping technologies: the good, the bad and the future, Energy Environ. Sci. 10 (9) (2017) 1885–1910.
[17] Z. Yu, Y. Yang, S. Yang, Q. Zhang, J. Zhao, Y. Fang, X. Hao, G. Guan, Iron-based oxygen carriers in chemical looping conversions: a review, Carbon Resour. Convers. 2 (2019) 23–34.
[18] L. Yu, W. Zhou, Z. Luo, H. Wang, W. Liu, K.e. Yin, Developing oxygen carriers for chemical looping biomass processing: challenges and opportunities, Adv. Sustain. Syst. 4 (12) (2020) 2000099.
[19] J. Zhang, T. He, Z. Wang, M. Zhu, K. Zhang, B. Li, J. Wu, The search of proper oxygen carriers for chemical looping partial oxidation of carbon, Appl. Energy. 190 (2017) 1119–1125.
[20] Z. Huang, Y. Zhang, J. Fu, L. Yu, M. Chen, S. Liu, F. He, D. Chen, G. Wei, K. Zhao, A. Zheng, Z. Zhao, H. Li, Chemical looping gasification of biomass char using iron ore as an oxygen carrier, Int. J. Hydrog. Energy. 41 (40) (2016) 17871–17883.
[21] X. Shen, F. Yan, Z. Zhang, C. Li, S. Zhao, Z. Zhang, Enhanced and environment-friendly chemical looping gasification of crop straw using red mud as a sinter-resistant oxygen carrier, Waste Manag. 121 (2021) 354–364.
[22] O. Condori, L.F. de Diego, F. Garcia-Labiano, M.T. Izquierdo, A. Abad, J. Adánez, Syngas production in a 1.5 kWth biomass chemical looping gasification unit using Fe and Mn ores as the oxygen carrier, Energy Fuels. 35 (21) (2021) 17182–17196.
[23] S. Yin, L. Shen, M. Dosta, E.-U. Hartge, S. Heinrich, P. Lu, J. Werther, T. Song, Chemical looping gasification of a biomass pellet with a manganese ore as an oxygen carrier in the fluidized bed, Energy Fuels. 32 (11) (2018) 11674–11682.
[24] K. Wang, Q. Yu, Q. Qin, L. Hou, W. Duan, Thermodynamic analysis of syngas generation from biomass using chemical looping gasification method, Int. J. Hydrog. Energy. 41 (24) (2016) 10346–10353.
[25] S. Wang, T. Song, S. Yin, E.-U. Hartge, T. Dymala, L. Shen, S. Heinrich, J. Werther, Syngas, tar and char behavior in chemical looping gasification of sawdust pellet in fluidized bed, Fuel. 270 (2020), 117464.
[26] J. Yan, T. Shen, P. Wang, X. Yin, X. Zhu, S. Jiang, L. Shen, Redox performance of manganese ore in a fluidized bed thermogravimetric analyzer for chemical looping combustion, Fuel. 295 (2021), 120564.
[27] Z. Deng, Z. Huang, F. He, A. Zheng, G. Wei, J. Meng, Z. Zhao, H. Li, Evaluation of calcined copper slag as an oxygen carrier for chemical looping gasification of sewage sludge, Int. J. Hydrog. Energy. 44 (33) (2019) 17823–17834.
[28] N. Dong, R. Huo, M. Liu, L. Deng, Z. Deng, G. Chang, Z. Huang, H. Huang, Chemical looping gasification of sewage sludge using copper slag modified by NiO as an oxygen carrier, Chin. J. Chem. Eng. 29 (2021) 335–343.
[29] Z. Huang, N.a. Gao, M. Liu, Y. Lin, G. Chang, L. Deng, H. Huang, Emissions of nitrogenous pollutants in chemical looping gasification of high nitrogen wood waste using a K-modified copper slag oxygen carrier, J. Therm. Anal. Calorim. 147 (17) (2022) 9725–9735.
[30] Y. Wang, M. Liu, N. Dong, Y. Lin, G. Chang, G. Wei, K. Zhao, X. Wang, A. Zheng, Z. Zhao, Chemical looping gasification of high nitrogen wood waste using a copper slag oxygen carrier modified by alkali and alkaline earth metals, Chem. Eng. J. 410 (2021), 128344.
[31] S. Fang, Z. Deng, Y. Lin, Z. Huang, L. Ding, L. Deng, H. Huang, Investigation of the nitrogen migration characteristics in sewage sludge during chemical looping gasification, Energy. 216 (2021), 119247.
[32] F. Hildor, H. Leion, C.J. Linderholm, T. Mattisson, Steel converter slag as an oxygen carrier for chemical-looping gasification, Fuel Process. Technol. 210 (2020), 106576.
[33] Z. Zhang, X. Wang, L. Zhang, H. Zhou, R. Ju, P. Rao, X. Guo, Y. Han, H. Chen, Characteristics of steel slag as an oxygen carrier for chemical looping gasification of sewage sludge, Energy. 247 (2022), 123534.
[34] F. Xu, X. Xing, S. Gao, W. Zhang, L. Zhu, Y. Wang, J. Chen, H. Chen, Y. Zhu, Direct chemical looping gasification of pine sawdust using Fe2O3-rich sludge ash as an oxygen carrier: thermal conversion characteristics, product distributions, and gasification performances, Fuel. 304 (2021), 121499.
[35] E. Ksepko, Sewage sludge ash as an alternative low-cost oxygen carrier for chemical looping combustion, J. Therm. Anal. Calorim. 116 (3) (2014) 1395–1407.
[36] Y. De Vos, M. Jacobs, P. Van Der Voort, I. Van Driessche, F. Snijkers, A. Verberckmoes, Development of stable oxygen carrier materials for chemical looping processes—a review, Catalysts. 10 (2020) 926.
[37] F. Li, H.R. Kim, D. Sridhar, F. Wang, L. Zeng, J. Chen, L.-S. Fan, Syngas chemical looping gasification process: oxygen carrier particle selection and performance, Energy Fuels. 23 (2009) 4182–4189.
[38] K.-S. Kang, C.-H. Kim, K.-K. Bae, W.-C. Cho, S.-H. Kim, C.-S. Park, Oxygen-carrier selection and thermal analysis of the chemical-looping process for hydrogen production, Int. J. Hydrog. Energy. 35 (22) (2010) 12246–12254.
[39] M. Tang, L. Xu, M. Fan, Progress in oxygen carrier development of methane-based chemical-looping reforming: a review, Appl. Energy. 151 (2015) 143–156.
[40] P. Morseletto, Targets for a circular economy, Resour. Conserv. Recycl. 153 (2020) 104553.
[41] S. Al-Busaltan, H. Al Nageim, W. Atherton, G. Sharples, Green bituminous asphalt relevant for highway and airfield pavement, Constr. Build. Mater. 31 (2012) 243–250.
[42] B. Das, S. Prakash, P.S.R. Reddy, V.N. Misra, An overview of utilization of slag and sludge from steel industries, Resour. Conserv. Recycl. 50 (1) (2007) 40–57.
[43] H. Purwanto, T. Akiyama, Hydrogen production from biogas using hot slag, Int. J. Hydrog. Energy. 31 (4) (2006) 491–495.
[44] B. Gorai, R.K. Jana, Premchand, Characteristics and utilisation of copper slag—a review, Resour. Conserv. Recycl. 39 (4) (2003) 299–313.
[45] J.-C. Lee, B.D. Pandey, Bio-processing of solid wastes and secondary resources for metal extraction–a review, Waste Manag. 32 (1) (2012) 3–18.
[46] S. Roudier, L.D. Sancho, R. Remus, M. Aguado-Monsonet, Best Available Techniques (BAT) reference document for iron and steel production: Industrial emissions directive 2010/75/EU: integrated pollution prevention and control, Joint Research Centre (Seville site), 2013.
[47] O. Condori, F. García-Labiano, F. Luis, M.T. Izquierdo, A. Abad, J. Adánez, Biomass chemical looping gasification for syngas production using LD Slag as oxygen carrier in a 1.5 kWth unit, Fuel Process. Technol. 222 (2021), 106963.
[48] Y.-L. Chen, M.-S. Ko, J.-E. Chang, C.-T. Lin, Recycling of desulfurization slag for the production of autoclaved aerated concrete, Constr. Build. Mater. 158 (2018) 132–140.
[49] X. Liu, P. Gao, Y. Han, Resource utilization of slag from desulphurization and slag skimming: a comprehensive recycling process of all components, Int. J. Min. Sci. Technol. 32 (2022) 585–593.
[50] M. Garside, World manganese reserves 2022, Statista. (2023). https://www.statista.com/statistics/247609/world-manganese-reserves/ (accessed February 16, 2023).
[51] M. Matzen, J. Pinkerton, X. Wang, Y. Demirel, Use of natural ores as oxygen carriers in chemical looping combustion: a review, Int. J. Greenh. Gas Control. 65 (2017) 1–14.
[52] L. Wei, F. Zhu, Q. Li, C. Xue, X. Xia, H. Yu, Q. Zhao, J. Jiang, S. Bai, Development, current state and future trends of sludge management in China: based on exploratory data and CO2-equivaient emissions analysis, Environ. Int. 144 (2020), 106093.
[53] J. Koppes, Solenis, Chang. Landsc, Sludge Dispos, 2022 https://www.solenis.com/en/resources/blog/the-changing-landscape-of-sludge-disposal (accessed January 21, 2023.
[54] J. de Brito, F. Agrela, New trends in eco-efficient and recycled concrete, Woodhead Publishing, 2018.
[55] Y. Li, V.G. Papangelakis, I. Perederiy, High pressure oxidative acid leaching of nickel smelter slag: characterization of feed and residue, Hydrometallurgy. 97 (2009) 185–193.
[56] A.-S.-G. Vilaplana, V.J. Ferreira, A.M. López-Sabirón, A. Aranda-Usón, C. Lausín-González, C. Berganza-Conde, G. Ferreira, Utilization of Ladle Furnace slag from a steelwork for laboratory scale production of Portland cement, Constr. Build. Mater. 94 (2015) 837–843.
[57] M. Arjmand, H. Leion, T. Mattisson, A. Lyngfelt, Investigation of different manganese ores as oxygen carriers in chemical-looping combustion (CLC) for solid fuels, Appl. Energy. 113 (2014) 1883–1894.
[58] F. Hildor, T. Mattisson, H. Leion, C. Linderholm, M. Rydén, Steel converter slag as an oxygen carrier in a 12 MWth CFB boiler–ash interaction and material evolution, Int. J. Greenh. Gas Control. 88 (2019) 321–331.
[59] Z. Huang, F. He, Y. Feng, K. Zhao, A. Zheng, S. Chang, G. Wei, Z. Zhao, H. Li, Biomass char direct chemical looping gasification using NiO-modified iron ore as an oxygen carrier, Energy Fuels. 28 (1) (2014) 183–191.
[60] H. Sun, Z. Wang, Y. Fang, Z. Liu, L. Dong, X. Zhou, Z. Yu, X. Li, J. Bai, J. Huang, A novel system of biomass for the generation of inherently separated syngas by combining chemical looping CO2-gasification and steam reforming process, Energy Convers. Manag. 251 (2022), 114876.

[61] W.K. Jozwiak, E. Kaczmarek, T.P. Maniecki, W. Ignaczak, W. Maniukiewicz, Reduction behavior of iron oxides in hydrogen and carbon monoxide atmospheres, Appl. Catal. Gen. 326 (1) (2007) 17–27.
[62] K.-S. Kang, C.-H. Kim, K.-K. Bae, W.-C. Cho, S.-U. Jeong, Y.-J. Lee, C.-S. Park, Reduction and oxidation properties of Fe2O3/ZrO2 oxygen carrier for hydrogen production, Chem. Eng. Res. Des. 92 (11) (2014) 2584–2597.
[63] J. Zieliński, I. Zglinicka, L. Znak, Z. Kaszkur, Reduction of Fe2O3 with hydrogen, Appl. Catal. Gen. 381 (1-2) (2010) 191–196.
[64] J. Hu, V.V. Galvita, H. Poelman, C. Detavernier, G.B. Marin, A core-shell structured Fe2O3/ZrO2@ ZrO2 nanomaterial with enhanced redox activity and stability for CO2 conversion, J. CO2 Util. 17 (2017) 20–31.
[65] F. Guo, X. Zhao, K. Peng, S. Liang, X. Jia, L. Qian, Catalytic reforming of biomass primary tar from pyrolysis over waste steel slag based catalysts, Int. J. Hydrog. Energy. 44 (31) (2019) 16224–16233.
[66] J. Wang, C. Zhang, Y. Wang, W. Chen, Z. Li, Y. Feng, The effect of synthesis methods on active oxygen species of mnox-cuo in soot combustion, Catal. Lett. 151 (11) (2021) 3261–3272.
[67] Y. Wang, P. Niu, H. Zhao, Chemical looping gasification of coal using calcium ferrites as oxygen carrier, Fuel Process. Technol. 192 (2019) 75–86, https://doi.org/10.1016/j.fuproc.2019.04.009.
[68] L. Xu, G.L. Schwebel, P. Knutsson, H. Leion, Z. Li, N. Cai, Performance of industrial residues as low cost oxygen carriers, Energy Procedia. 114 (2017) 361–370.
[69] X. Zhu, Y. Wei, H. Wang, K. Li, Ce–Fe oxygen carriers for chemical-looping steam methane reforming, Int. J. Hydrog. Energy. 38 (11) (2013) 4492–4501.
[70] X.P. Dai, R.J. Li, C.C. Yu, Z.P. Hao, Unsteady-state direct partial oxidation of methane to synthesis gas in a fixed-bed reactor using AFeO3 (A= La, Nd, Eu) perovskite-type oxides as oxygen storage, J. Phys. Chem. B. 110 (45) (2006) 22525–22531.
[71] S. Bhavsar, G. Veser, Chemical looping beyond combustion: production of synthesis gas via chemical looping partial oxidation of methane, Rsc Adv. 4 (2014) 47254–47267.
[72] D. Jing, Innovative oxygen carriers for chemical-looping combustion, Chalmers University of Technology Gothenburg, Sweden, 2015.
[73] M. Rydén, P. Moldenhauer, S. Lindqvist, T. Mattisson, A. Lyngfelt, Measuring attrition resistance of oxygen carrier particles for chemical looping combustion with a customized jet cup, Powder Technol. 256 (2014) 75–86.
[74] J.H. Siegell, High-temperature de fluidization, Powder Technol. 38 (1) (1984) 13–22.
[75] P. Compo, R. Pfeffer, G.I. Tardos, Minimum sintering temperatures and defluidization characteristics of fluidizable particles, Powder Technol. 51 (1) (1987) 85–101.
[76] D.L. Keairns, Fluidization technology, Hemisphere Publishing Corporation, 1976.
[77] J. Shao, D.H. Lee, R. Yan, M. Liu, X. Wang, D.T. Liang, T.J. White, H. Chen, Agglomeration characteristics of sludge combustion in a bench-scale fluidized bed combustor, Energy Fuels. 21 (5) (2007) 2608–2614.
[78] R.W. Bryers, Fireside slagging, fouling, and high-temperature corrosion of heat-transfer surface due to impurities in steam-raising fuels, Prog. Energy Combust. Sci. 22 (1) (1996) 29–120.
[79] S.V. Vassilev, K. Kitano, S. Takeda, T. Tsurue, Influence of mineral and chemical composition of coal ashes on their fusibility, Fuel Process. Technol. 45 (1) (1995) 27–51.
[80] R. Yan, D.T. Liang, K. Laursen, Y. Li, L. Tsen, J.H. Tay, Formation of bed agglomeration in a fluidized multi-waste incinerator☆, Fuel. 82 (7) (2003) 843–851.
[81] Z. Zhang, X. Wu, T. Zhou, Y. Chen, N. Hou, G. Piao, N. Kobayashi, Y. Itaya, S. Mori, The effect of iron-bearing mineral melting behavior on ash deposition during coal combustion, Proc. Combust. Inst. 33 (2) (2011) 2853–2861.
[82] B.-M. Steenari, O. Lindqvist, V. Langer, Ash sintering and deposit formation in PFBC, Fuel. 77 (5) (1998) 407–417.
[83] D.M. Mason, J.G. Patel, Chemistry of ash agglomeration in the U-GAS® process, Fuel Process. Technol. 3 (3-4) (1980) 181–206.
[84] D.N. Aditya, M. Maria, P. Hilde, T. Stuart, D. Christophe, Deactivation Study of Fe2O3–CeO2 during Redox Cycles for CO Production from CO2, (2016).
[85] N.V.R.A. Dharanipragada, M. Meledina, V.V. Galvita, H. Poelman, S. Turner, G. Van Tendeloo, C. Detavernier, G.B. Marin, Deactivation study of Fe2O3–CeO2 during redox cycles for CO production from CO2, Ind. Eng. Chem. Res. 55 (20) (2016) 5911–5922.
[86] V. Galvita, T. Hempel, H. Lorenz, L.K. Rihko-Struckmann, K. Sundmacher, Deactivation of modified iron oxide materials in the cyclic water gas shift process for CO-free hydrogen production, Ind. Eng. Chem. Res. 47 (2) (2008) 303–310.
[87] M. Thaler, V. Hacker, M. Anilkumar, J. Albering, J. Besenhard, H. Schrottner, M. Schmied, Investigations of cycle behaviour of the contact mass in the RESC process for hydrogen production, Int. J. Hydrog. Energy. 31 (14) (2006) 2025–2031.
[88] S. Takenaka, K. Nomura, N. Hanaizumi, K. Otsuka, Storage and formation of pure hydrogen mediated by the redox of modified iron oxides, Appl. Catal. Gen. 282 (1-2) (2005) 333–341.
[89] M. Schmid, S. Hafner, G. Scheffknecht, Experimental parameter study on synthesis gas production by steam-oxygen fluidized bed gasification of sewage sludge, Appl. Sci. 11 (2021) 579.